Available online at www.sciencedirect.com

ScienceDirect

Journal of Magnesium and Alloys 11 (2023) 176–191

www.elsevier.com/locate/jma

Full Length Article

Local hardening and asymmetric twin growth by twin-twin interactions in a Mg alloy

Krishna Yaddanapudi[a], Mariyappan Arul Kumar[b,*], Jiaxiang Wang[c], Xin Wang[d], Timothy J. Rupert[d], Enrique J. Lavernia[d], Julie M. Schoenung[d], Irene J. Beyerlein[c,e], Subhash Mahajan[a]

[a] *Department of Materials Science and Engineering, University of California, Davis, CA 95616, USA*
[b] *Materials Science and Technology Division, Los Alamos National Laboratory, Los Alamos, NM 87545, USA*
[c] *Department of Mechanical Engineering, Materials Department, University of California, Santa Barbara, CA 93106, USA*
[d] *Department of Materials Science and Engineering, University of California, Irvine, USA*
[e] *Materials Department, University of California, Santa Barbara, CA 93106, USA*

Received 12 September 2022; received in revised form 3 November 2022; accepted 10 November 2022
Available online 8 December 2022

Abstract

In this study, the role of twin-twin interactions on the distributions of local defects (e.g., dislocations) and stress fields in a magnesium alloy is investigated. A co-zone $(10\bar{1}2)$-$(\bar{1}012)$ tensile twin junction in a deformed Mg-3wt.%Y alloy is analyzed using transmission electron microscopy (TEM). The results show that the morphology of the impinging $(\bar{1}012)$ twin is asymmetric, and the non-interacting boundary of the recipient $(10\bar{1}2)$ twin is irregular. Detailed analysis of TEM images reveals that type-II pyramidal $[\bar{1}2\bar{1}3](1\bar{2}12)$ dislocations concentrate in the vicinity of the twin-twin junction site. The same $\langle c + a\rangle$ dislocations are also observed inside the interacting twin domains along with a few $\langle a\rangle$ dislocations. The $\langle c + a\rangle$ dislocations emanating from the impinging $(\bar{1}012)$ twin boundary have edge character and are extended with faults parallel to the basal plane. In contrast, the $\langle c + a\rangle$ dislocations connected to the recipient $(10\bar{1}2)$ twin are predominantly screw orientation and compact. Elasto-viscoplastic fast Fourier transform based crystal plasticity calculations are performed to rationalize the observed twin morphology and local dislocation distribution. The model calculations suggest that the local stress fields generated at the junction site where the two twins meet are responsible for the experimentally observed concentration of $\langle c + a\rangle$ dislocations. The calculated stress fields are asymmetric with respect to the junction site, explaining the observed asymmetric morphology of the impinging twin. Overall, these findings show strong effects of twin-twin interactions on the distribution of dislocations as well as the evolution of the twinned microstructure and as such, can help advance understanding of twinning in Mg alloys and their effect on mechanical behavior.

Keywords: Tensile twins; Twin-twin intersections; Mg alloys; Crystal plasticity; TEM.

1. Introduction

Magnesium and its alloys are highly attractive materials for many engineering applications due to their low density and high specific strength [1]. Due to the hexagonal close-packed (HCP) crystal structure of Mg, both dislocation slip and deformation twinning can be readily activated [2,3]. Different twinning modes can be activated based on the loading direction with respect to the crystal orientation. For instance, tensile and compression twins will be activated when the c-axis of the crystal experiences tension and compression loading, respectively. In Mg, the activation of $\{10\bar{1}2\}$ tensile twinning is abundant compared to the other twin modes [4,5]. In an HCP crystal, the $\{10\bar{1}2\}$ tensile twin has six crystallographically equivalent variants. Often, multiple non-parallel

---

[*] Corresponding author.
E-mail address: marulkr@lanl.gov (M.A. Kumar).

https://doi.org/10.1016/j.jma.2022.11.008

variants are activated within a grain/crystal, and their activation depends on the stress state. For example, c-axis tension can equally activate all six variants, whereas the compression normal to the prismatic plane can activate only two equally stressed variants. Thus, the deformation behavior of Mg and its alloys is mainly governed by dislocation-dislocation [6–10], dislocation-twin [11–15], and twin-twin [16] interactions. The interaction between dislocations in HCP magnesium is complex and significantly affects the macroscopic anisotropic response of the material. For instance, the interaction between basal ⟨a⟩ and pyramidal ⟨c + a⟩ dislocations is stable and strong compared to the interaction of second order pyramidal ⟨c + a⟩ dislocations [17]. Similarly, the interaction between twins and dislocations also greatly affects the mechanical response and microstructure of the HCP metals. For example, the interaction between basal ⟨a⟩ dislocations and tensile twin boundaries in magnesium creates twinning dislocations that help the migration of twin boundaries [13–15,18–21]. Also, the interaction of dislocations with a twin boundary develops new defects within and in the vicinity of twins. For instance, the transmutation reactions of matrix ⟨a⟩ dislocations with tensile twin boundaries develops ⟨c + a⟩ dislocations [12,22]. The twin-dislocation interaction has been studied extensively for pure Mg [14,15] and its alloys containing Al, Zn, Li, Y, and so on [11,13,18,22–29]. Compared to dislocation-dislocation and dislocation-twin interactions, twin-twin interactions remain poorly understood and are the focus of the present work.

Non-parallel twin interactions create twin-twin junctions (TTJ). Based on the crystallographic misorientation between the two interacting twins, twin-twin junctions can be categorized into two types: cozone (two twins share the same zone axis) and non-cozone [30]. In the latter, the intersecting twins do not share the same zone axis and the angle between the zone axes will be either $2\pi/3$ or $\pi/3$. Both cozone and non-cozone interactions are observed in Mg and its alloys and hence believed to significantly affect microstructural evolution and materials performance [31–37]. TTJs, for example, have been identified as nucleation sites for dislocations, twins, and cracks [32,38,39]. The local stress/strain fields and defects associated with TTJs can potentially control the growth of interacting twins [40,41]. Lloyd et al. recently showed that the presence of TTJs significantly alters the microstructure under shock loading in Mg [42]. Specifically, they found that the interaction of newly formed twins with the pre-existing TTJs changes twin formation into an irreversible process. When the annealed Mg alloy is subjected to rolling direction (RD) compression, newly formed deformation twins do not have enough time to interact with defects like dislocations, and so twinning becomes nearly reversible. On the other hand, in the pre-strained sample, which already contains TTJs, the shock loading-induced twins interact with the pre-existing TTJs and develop a stable twinned microstructure. Consequently, any newly formed twins became irreversible and retained after shock recovery. Recent work by Zhang et al. reveals that the presence of TTJs can promote recrystallization, helping to weaken the texture and achieve uniform grain growth in Mg alloys [43]. It has also been well documented that the presence of TTJs strongly affects material strength and strain hardening response, mainly under cyclic loading [32,33,39]. Yu et al. showed that the yield strength and strain hardening rate increases with the loading cycles, which is directly correlated with an increase in the number of TTJs [33]. Thus, the understanding of TTJ formation, growth of interacting twins, and the local defects present within and around the junctions is of paramount importance.

In recent years, twin-twin interactions in HCP metals have been studied via *in-situ/ex-situ* experiments and numerical simulations [33,35,36,40,44]. Most studies investigate the structural characteristics of the TTJ, mainly the twin-twin boundaries (TTB) associated with junctions [33,35,36,40]. For both cozone and non-cozone junctions, three interfaces are commonly observed: the interface (i) on the obtuse or (ii) acute side of the junction, or (iii) parallel to the receiving twin crystallographic plane. The cozone interaction is shown to create interfaces parallel to the basal and prismatic planes of both twins, and to the $\{10\bar{1}2\}$ plane of the recipient twin. Only a few studies attempted to quantify the local stresses associated with TTJs. Using a crystal plasticity framework and molecular dynamics simulations, Arul Kumar et al. calculated the stresses within and around the cozone TTJ in Mg [41]. The calculated stress fields show that the TTJs are formed by migrating both the impinging and recipient twin boundaries. The TTJs can form a new twin on the other side of the recipient twin, which leads to the experimentally observed apparent crossing structure. Using atomistic calculations, Gong et al. showed that the local stresses on the obtuse and acute sides of the non-cozone TTJ are different, and can lead to asymmetric growth of the interacting twins [40]. With these studies, the structural characteristics and local stresses associated with TTJ are understood to some extent. However, to understand twin-twin interactions completely, the local defects present inside and around the junctions and their interaction with twin domains need to be explored. To the best of our knowledge, none of the existing literature reports on such local defects to the desired level of detail.

In this work, transmission electron microscopy (TEM) diffraction and related contrast imaging techniques are employed to characterize the defect structure inside and around a co-zone TTJ in an Mg-3wt.%Y alloy. The detailed analysis reveals many important findings: (i) pyramidal ⟨c + a⟩ dislocations concentrate near TTJ in the matrix grain; (ii) the same pyramidal ⟨c + a⟩ dislocations develop inside both twin domains; and (iii) the morphology of the impinging twin is asymmetric. To understand and rationalize the experimental observations, fast Fourier transform-based crystal plasticity modeling is performed. The model calculation shows that the interaction between twins introduces more pyramidal ⟨c + a⟩ dislocations in the vicinity of the junction in the matrix grain. Experimentally observed dislocations inside the twin domains are mostly likely developed during macroscopic loading. The model calculated stress field is asymmetric about the impinging twin and thus explains the experimentally observed asymmetric twin morphology.

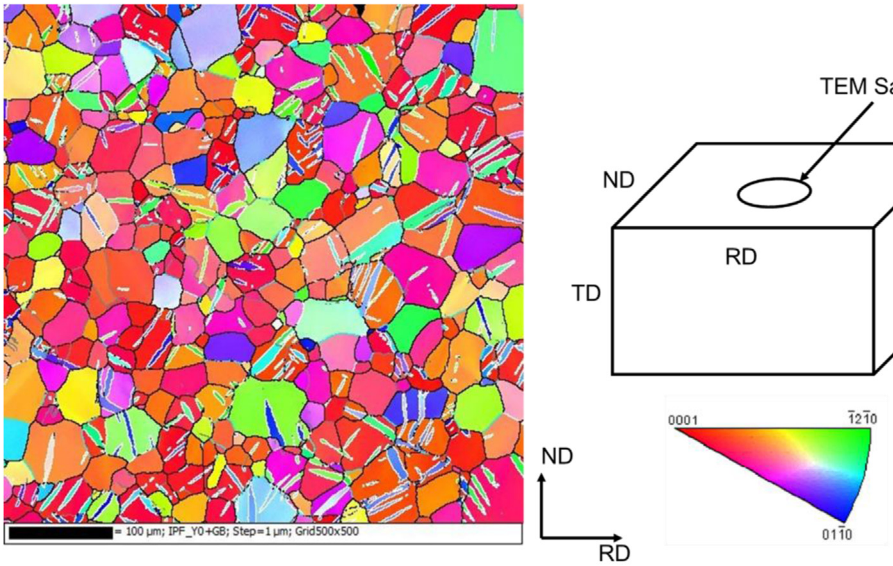

Fig. 1. A typical electron backscatter diffraction (EBSD) inverse pole figure (IPF) image of Mg-3wt.%Y alloy, which is deformed in compression along the RD. The schematic shows the macroscopic sample directions of the alloy in relation to the transmission electron microscope (TEM) foil preparation. Here RD, TD and ND refer to rolling, transverse and normal directions, respectively.

2. Experimental methods

In this work, Mg-3wt.%Y alloy is selected to investigate the twin-twin interactions and associated defects. It has been well recognized that the addition of rare-earth element Y improves the strength and ductility of the magnesium alloy by increasing the pyramidal ⟨c + a⟩ activity via lowering the I1 stacking fault energy and by increasing the barrier for tensile twinning [45–47]. Further, in our recent study, the mechanical properties and the evolution of crystallographic texture of Mg-3wt.%Y alloy are studied [48]. It provides the material data for the EVP-FFT calculation, which is set up in the next section. Mg-3wt.%Y alloys were obtained from the Helmholtz-Zentrum Geesthachat Center for Materials and Costal Research. Prior to recrystallization at 450 °C for 10 min, the homogenization of cast ingots and hot rolling were performed at 500 °C. The annealing resulted in a fully recrystallized twin-free microstructure with an average grain size of 26 μm. Subsequently, the annealed rolled sheet was sectioned using electrical discharge machining (EDM) to make cuboids of dimensions 3.3 × 3.3 × 5.0 mm with the longest dimension along the rolling direction (RD). The cuboids were then deformed in compression at ambient temperature to an engineering strain of 2% along the RD at a strain rate of $\sim 10^{-3}\ \mathrm{s}^{-1}$ using 8801 servo-hydraulic universal testing equipment (Instron Inc., USA). Refer to [48] for a detailed description of the material and mechanical testing procedures.

The microstructure of the deformed Mg-3wt.%Y alloy samples was examined using a JEOL JEM 2100F-AC TEM, operating at 200 kV. The TEM samples were prepared using an FEI Scios dual-beam focused ion beam (FIB) equipped with a Ga-ion source. The prepared TEM samples and its corresponding orientation with respect to the sample coordinate system are provided in Fig. 1. The crystallography of grains and twins present in the TEM samples was studied by analyzing the observed selected area electron diffraction (SAED) patterns. Characteristics of the dislocations in the TEM samples were examined using the invisibility criteria, where a perfect lattice dislocation becomes invisible when the vector product $g.b = 0$, where g is the operating reflection used and b is the corresponding Burgers vector of the dislocation. The glide (habit) planes of the dislocations (twins) were identified from the observed diffraction patterns coupled with surface trace analysis.

Fig. 1 shows a typical EBSD inverse pole figure (IPF) image of the deformed Mg-3wt.%Y alloy, which contains grains and individual twins, as well as TTJs formed across some grains. The normal to the image plane is oriented along the macroscopic transverse direction (TD) of the sample. The schematic shows the relation between the macroscopic sample directions and the region that was used for TEM sample preparation. The normal to the TEM sample is oriented along the TD of the sample.

3. Numerical methods

In this work, an elasto-visco-plastic fast Fourier transform (EVPFFT) based crystal plasticity model is employed to calculate the local stresses and dislocation fields associated with a twin-twin interaction in Mg-Y alloy. Here, the formulation that combines the original EVPFFT framework [49] with inclusion of discrete intragranular twin domains [41,50,51] and with dislocation density (DD) based hardening for the critical resolved stress of each slip system [52] is used. Before performing the twin-twin interaction calculations, as a first

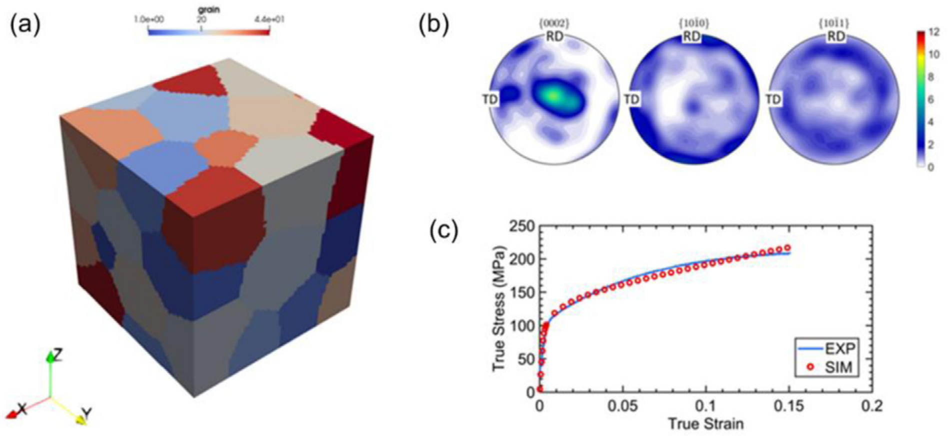

Fig. 2. (a) Polycrystal model for calibrating dislocation density-based hardening model parameter; (b) initial texture for the polycrystal model; (c) model predicted strain-stress response for rolling direction tension along with the experimental data [48].

Table 1
Calibrated dislocation density-based hardening model parameters for Mg-3%Y. Here $\boldsymbol{\tau}_0^{\boldsymbol{\alpha}}$, $\mathbf{k}_0^{\boldsymbol{\alpha}}$, D, **g** and Q refer to initial lattice friction, dislocation generation rate, drag stress, normalized stress-independent activation energy, and rate coefficient for dislocation debris formation, respectively. For more details, refer to [52].

	τ_0^α (MPa)	k_0^α (m^{-1})	D (MPa)	g	Q
Basal	18	1.5e9	3500	0.003	20
Prismatic	65	8e8	6000	0.002	0
Pyramidal	88	6e8	3300	0.002	29.6

step, the DD model parameters are identified using the experimentally measured stress-strain responses of the Mg-3wt.%Y alloy. Recently, using the effective medium visco-plastic self-consistent (VPSC) framework, Wang et al. [48] obtained the DD model parameters for the same material system. Thus, the model parameter calibration process is started from the parameters listed in [48] and adjusted them to capture the experimental stress-strain curves using the EVPFFT framework. Deformation at every material point in the EVPFFT model is carried by a combination of anisotropic elasticity and crystallographic slip-mediated visco-plasticity. The anisotropic elastic constants (in GPa) of the simulated material are taken as: $C_{11} = 59.5$, $C_{12} = 26.1$, $C_{13} = 21.8$, $C_{33} = 65.6$ and $C_{44} = 16.3$ [53]. Plasticity is assumed to be accommodated by basal ⟨a⟩, prismatic ⟨a⟩, and pyramidal-II ⟨c + a⟩ slip modes. The initial dislocation density for each slip system is assumed to be 10×10^{10} m^{-2}. A 3D polycrystalline microstructure with 44 equiaxed grains was made through Dream3D, see Fig. 2(a). The distribution of the initial crystallographic orientation of the grains is shown in Fig. 2(b). The model unit cell is discretized into 60 × 60 × 60 voxels. Uniaxial tension along the rolling direction is simulated at a strain rate of 1.0×10^{-3} s^{-1}. The model predicted stress-strain response along with the experimental data is shown in Fig. 2(c). For the parameter set listed in Table 1, the model response shows good agreement with the experiment [48]. This DD model parameter set was used in the following explicit TTJ simulation, which is discussed later.

3. Results

3.1. Cozone twin-twin interaction

Fig. 3(a) shows the weak beam dark field (WBDF) TEM micrograph of the deformed Mg-3wt.%Y alloy consisting of two grains labeled as G1 and G2. Grain G2 is out of contrast and the white dashed line highlights the grain boundary. Grain G1 contains two twins labeled as T1 and T2. Twin T2 terminates at the boundary of twin T1, whereas twin T1 terminates at the grain boundary. Twins T1 and T2 interact and form a TTJ. Both twins are highlighted by the white dashed lines for clarity. Based on the observed configuration, hereinafter, twins T1 and T2 are referred to as the recipient and impinging twins, respectively.

Fig. 3(b) shows a bright field TEM image of a portion of the two grains (indicated by a white circle in Fig. 3(a)) along with the observed SAED pattern, which is acquired from a region enclosed by a small circle on the micrograph. The SAED pattern consists of diffraction spots belonging to both grains. These spots have been carefully identified and are represented by white (G2) and orange (G1) colored grids in Fig. 3(b). The SAED patterns acquired from the individual grains are also provided for comparison. The SAED analysis confirms that G1 is oriented along the $[1\bar{2}10]$ direction while G2 is oriented along the $[\bar{2}\bar{5}7\bar{3}]$ direction. Both crystallographic directions are parallel to the macroscopic TD of the sample. A simulated diffraction pattern

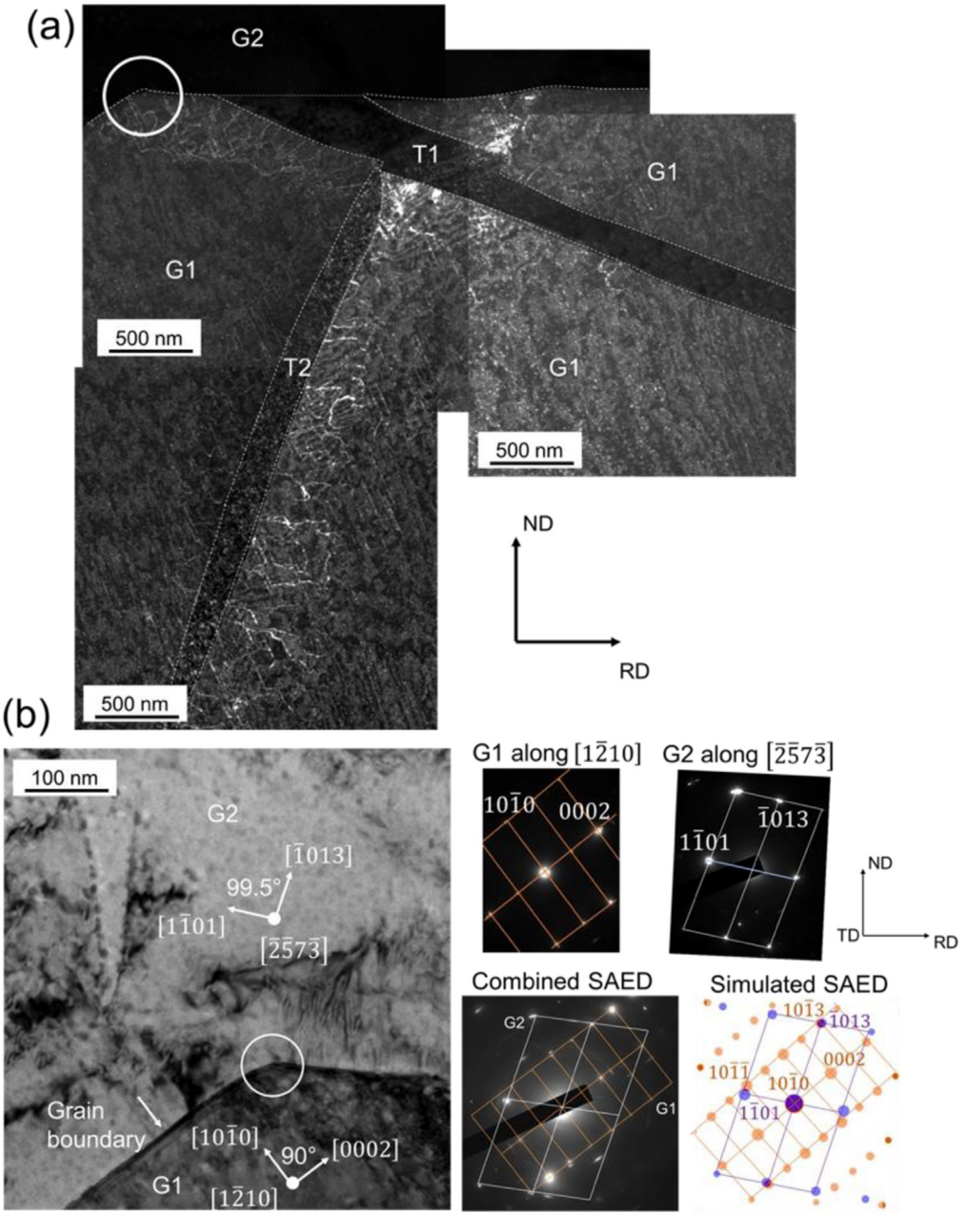

Fig. 3. (a) A WBDF TEM micrograph showing the two grains G1 and G2. The G1 contains a twin-twin junction, where twin T1 is terminated at the grain boundary and twin T2 is terminated at T1 boundary. (b) A bright field TEM image showing a small portion of two grains (indicated by a white circle in (a)) along with a combined experimental SAED pattern acquired from a region enclosed by a small white circle. In the combined experimental SAED pattern, the white grid represents G2 spots, and the orange grid outlines the spots corresponding to G1. A corresponding simulated pattern is also provided, where the orange spots represent G1 and the blue spots represent G2. The individual SAED patterns acquired from the regions of G1 and G2 are also provided for clarity, where G1 is along the $[1\bar{2}10]$ orientation and G2 is along the $[\bar{2}\bar{5}7\bar{3}]$ orientation.

is also shown in Fig. 3. The SAED analysis indicates that the $(10\bar{1}3)$ crystallographic plane of G1 closely matches the $(\bar{1}013)$ crystallographic plane of G2.

To characterize the crystallography of these twins, Fig. 4 shows a WBDF TEM image along with the experimentally observed SAED patterns of a small region of G1 that comprises the TTJ. The patterns confirm that G1 is oriented along the $[1\bar{2}10]$ orientation, whereas T1 and T2 are oriented along the $[\bar{1}2\bar{1}0]$ direction. The symmetry of diffraction patterns confirms that the twins T1 and T2 are $\{10\bar{1}2\}$ type tensile twins. The yellow box in the SAED patterns outline the spots corresponding to the matrix (i.e., G1), whereas the red boxes represent the spots belonging to the recipient and impinging twins. The subsequent SAED analysis coupled with the trace analysis confirms that $(10\bar{1}2)$ and $(\bar{1}012)$ are the habit planes of T1 and T2. Their habit planes are rotated by 87° about the cozone axis $[1\bar{2}10]$. Thus, the observed TTJ is a cozone type interaction. Importantly the morphology of the impinging twin T2 is not symmetric and many matrix dislocations interact with the twin-matrix interfaces in Fig. 4. The

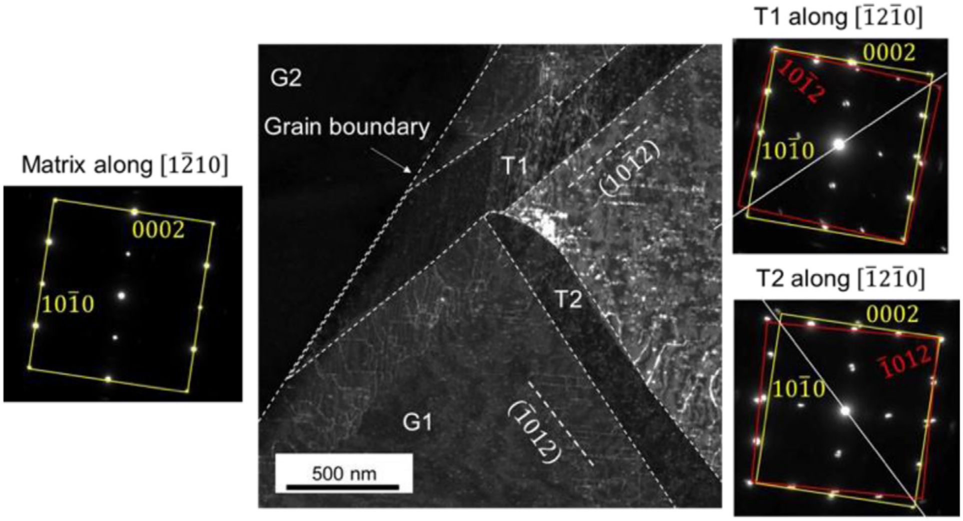

Fig. 4. A WBDF TEM image of a small region in G1 that consists of both T1 and T2 twins. The observed SAED patterns confirm that both T1 and T2 are of $\{10\bar{1}2\}$ tensile twins. Further, the morphology of the impinging twin T2 is asymmetric. In the SAED patterns the yellow-colored boxes outline the spots corresponding to the matrix whereas the red-colored boxes outline the spots corresponding to twins T1 and T2. The white-colored dashed lines represent the traces of habit planes of T1 and T2.

Table 2
The magnitudes of g•b values used in this study.

	$\pm\frac{1}{3}[11\bar{2}3]$	$\pm\frac{1}{3}[\bar{1}2\bar{1}3]$	$\pm\frac{1}{3}[\bar{2}113]$	$\pm\frac{1}{3}[11\bar{2}\bar{3}]$	$\pm\frac{1}{3}[\bar{1}2\bar{1}\bar{3}]$	$\pm\frac{1}{3}[\bar{2}11\bar{3}]$
0002	± 2	± 2	± 2	∓2	∓2	∓2
$10\bar{1}0$	± 1	0	∓1	± 1	0	∓1
$10\bar{1}1$	± 2	± 1	0	0	∓1	∓2
$10\bar{1}\bar{1}$	0	∓1	∓2	± 2	± 1	0
$0\bar{1}11$	0	0	∓1	± 2	± 2	± 1

subsequent sections investigate the character of these dislocations in detail and whether the asymmetry was induced after the intersection occurred.

3.2. Dislocations in the vicinity of TTJ

Fig. 5(a) shows a WBDF image of the matrix grain in the vicinity of TTJ. It clearly reveals that the dislocations in the matrix grain interact with the boundaries of both the impinging and recipient twins. It is evident that dislocation lines are projected in different directions on the plane of the micrograph. The character of these dislocations has been examined by TEM dislocation contrast experiments in Fig. 5(c) and (d) using various operating reflections and under the $[1\bar{2}10]$ and $[11\bar{2}3]$ zone axes conditions. The red arrows indicate the contrast variation from a few specific dislocations for the operating reflections used. Furthermore, the dislocations (see Fig. 5(a)) exhibit a line contrast for the reflection $g = 0002$, suggesting that they have a strong $\langle c \rangle$-component. The dislocation contrast experiments in Fig. 5(c) and (d) infer that the interacting matrix dislocations are mixed (i.e., $\langle c + a \rangle$) and satisfying the Burgers vector of $b_m = \frac{1}{3}[\bar{1}2\bar{1}3]$. The corresponding g•b values for these dislocations are tabulated in Table 2.

Fig. 5(a) also shows that the horizontal $\langle c + a \rangle$ dislocation line segments project along the $[\bar{1}010]$ direction on the basal plane, while the vertical line $\langle c + a \rangle$ segments lie out of the basal plane. Earlier studies based on TEM reported a similar $\langle c + a \rangle$ dislocation contrast parallel to the basal plane for pure Mg and Mg-Y and Mg-Li alloys [26,45,54,55]. The origin of such a contrast can be observed from the $\langle c + a \rangle$ dislocations gliding on type-II pyramidal planes [26,45,54,55]. Here, the SAED and trace analysis suggests that the matrix $\langle c + a \rangle$ dislocations in Fig. 5(a) lie on the type-II pyramidal plane $(1\bar{2}12)$ and satisfy the following slip system: $\frac{1}{3}[\bar{1}2\bar{1}3](1\bar{2}12)$. The $\langle c + a \rangle$ dislocations gliding on the $(1\bar{2}12)$ plane may be blocked at the line of intersection with the basal plane as illustrated in the schematic in Fig. 5(b) and produce a dislocation contrast parallel to the $[\bar{1}010]$ direction on the basal plane. Moreover, the $\langle c + a \rangle$ dislocations blocked at this line of intersection are in edge orientation because the line of intersection (i.e., $[\bar{1}010]$) is perpendicular to the observed Burgers vector ($\frac{1}{3}[\bar{1}2\bar{1}3]$). In contrast, the vertical segments of $\langle c + a \rangle$ dislocations are found to be in near-screw orientation as shown in Fig. 5(a). Further, it reveals that these matrix $\langle c+a \rangle$ dislocations interact with the tensile twin boundaries in a particular orientation. The $\langle c + a \rangle$ dislocations interacting with the T1 twin boundary are predominantly in screw

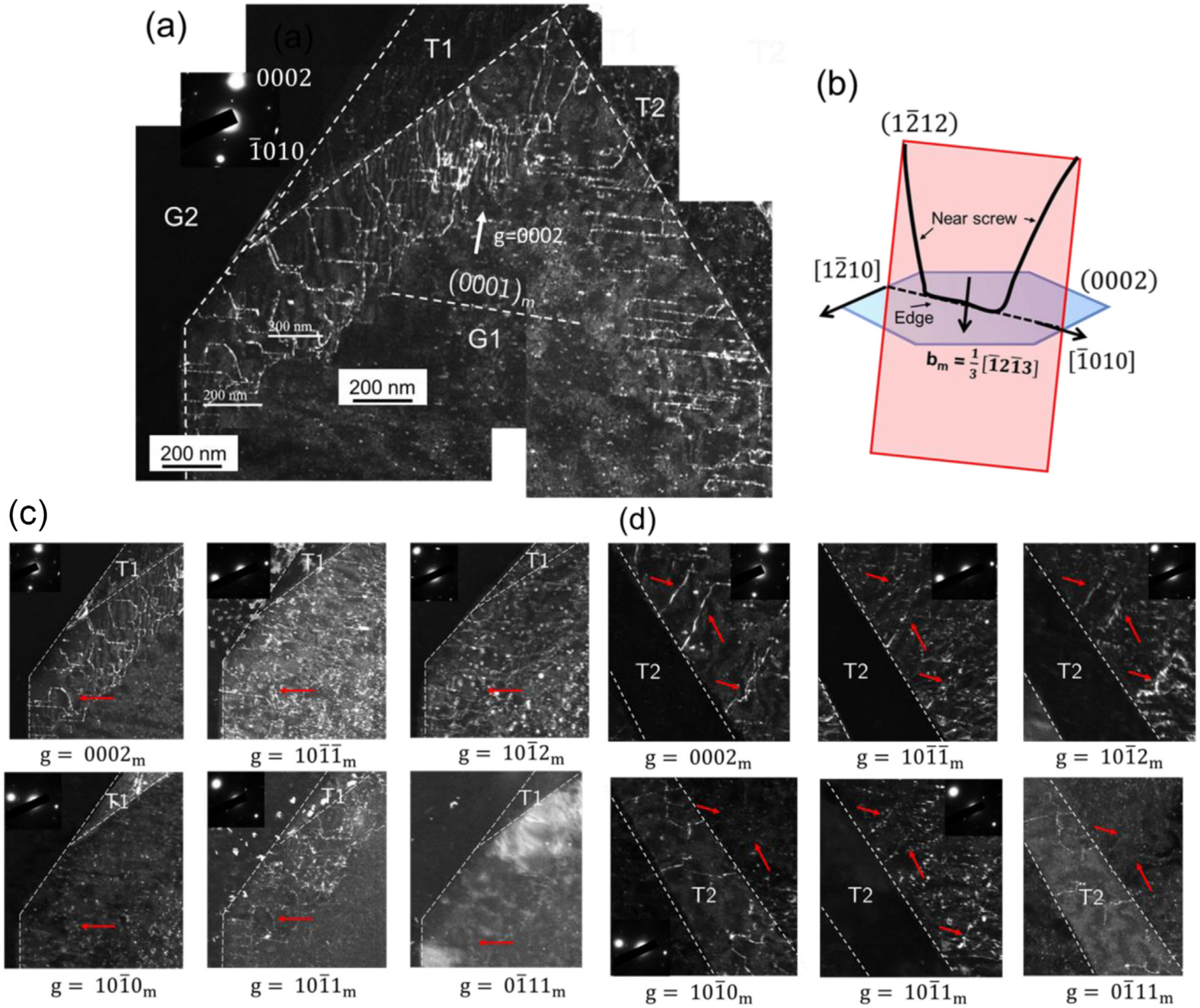

Fig. 5. (a) a WBDF TEM image shows the interaction of matrix $\langle c + a \rangle$ dislocations with the boundaries of T1 and T2. (b) The schematic demonstrates the observed $\langle c + a \rangle$ dislocations in near screw and edge orientations on type-II pyramidal plane i.e., $(1\bar{2}12)$. The WBDF images in (c) and (d) show the dislocation contrast variation in the vicinity of T1, T2, and for several operating reflections 'g' provided for each image. The red arrows point to the contrast variation from a few specific dislocations.

orientation, whereas the $\langle c + a \rangle$ dislocations interacting with the T2 twin boundary are predominantly in edge orientation.

The edge $\langle c + a \rangle$ dislocations were found to exhibit a stacking fault contrast. Fig. 6 shows the WBDF TEM images of the same twin-twin intersection under two different diffraction conditions. It should be noted that the dislocation contrast in Fig. 6(a) for the $g = 0002$ reflection exhibits a sharp line contrast. However, when the sample is slightly tilted about the $[\bar{1}010]$ axis, a stacking fault loop contrast on the basal plane is evident along the $[\bar{1}010]$ direction as indicated by the red arrows in Fig. 6(b), suggesting that the edge $\langle c + a \rangle$ dislocations may be dissociated into partial dislocations bounding the stacking faults. In contrast to the edge $\langle c + a \rangle$ dislocations, the near-screw $\langle c + a \rangle$ dislocations do not exhibit such a stacking fault contrast, as confirmed by the absence of non-basal stacking fault contrast in Fig. 6(b). The same conclusions can be made in Fig. 6(c), where the $\langle c + a \rangle$ dislocations interacting with the T2 twin tip also exhibit basal stacking fault contrast. From Fig. 6(b) the stacking fault density is higher at the T2 twin boundary. This is because the $\langle c + a \rangle$ dislocations interacting with the T2 twin are predominantly in edge orientation (see Fig. 6(a)), while the $\langle c + a \rangle$ dislocations interacting with the T1 are predominantly screw character. As before, these screw $\langle c + a \rangle$ dislocations are not widely dissociated enough to show any stacking fault contrast. Consequently, the stacking fault density is lower on the T1 side.

In summary, $\frac{1}{3}[\bar{1}2\bar{1}3](1\bar{2}12)\langle c + a \rangle$ matrix dislocations lie on the type-II pyramidal plane and interact with both the T1 and T2 twins of the TTJ. These dislocations are observed in both edge and screw orientations. The edge components interact predominantly with the T2 twin boundary, whereas the

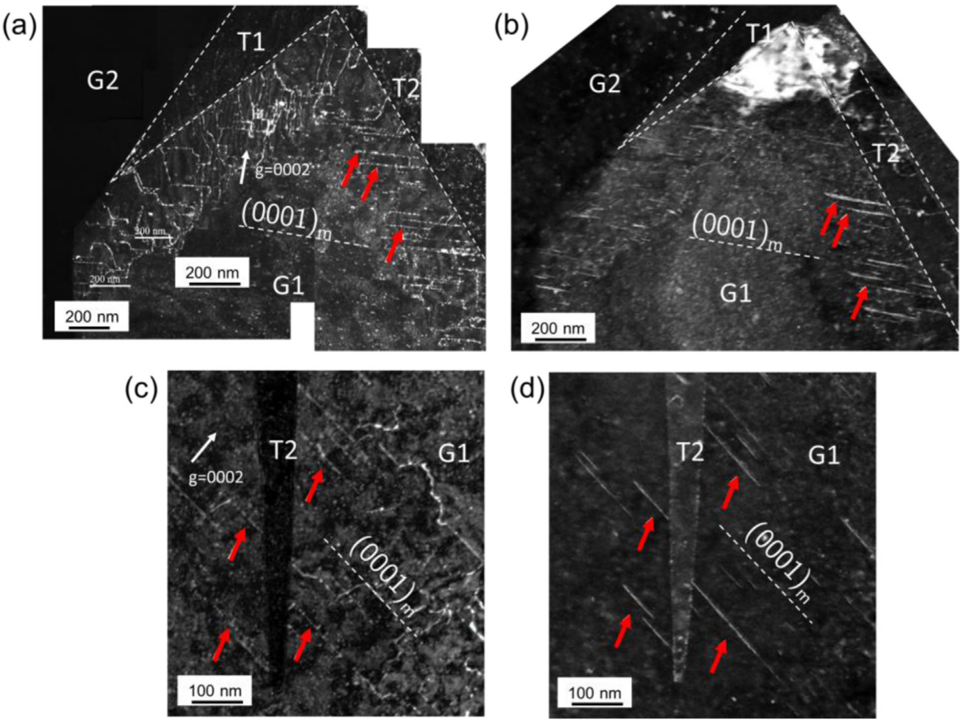

Fig. 6. WBDF TEM images (a) and (c) show the projected line segments of $\langle c + a \rangle$ dislocations both parallel and non-parallel to the basal plane for the reflection $g = 0002$. The dislocations parallel to the basal plane are in edge orientation as described in the schematic (Fig. 5b). However, after a slight tilt about the $[\bar{1}010]$ axis in (b) and (d), these dislocations exhibit stacking fault contrast parallel to the basal plane, whereas non-basal components are disappeared. The red arrows point to the contrast variation for a few specific dislocations before and after a slight tilt about the $[\bar{1}010]$ axis.

screw components interact predominantly with the T1 twin boundary. Moreover, the edge components exhibit a stacking fault contrast parallel to the trace of the basal plane. In contrast, $\langle a \rangle$ dislocations were not observed, which can be expected due to the grain orientation.

3.3. Defect structures within the twin domains

Similar TEM diffraction contrast experiments have been performed to investigate the defects present inside tensile twins T1 and T2. From the SAED patterns described in Fig. 4, the $g = 10\bar{1}0$ reflection of the matrix overlaps with the $g = 0002$ reflection of twins and vice versa, due to the crystallographic tensile twin/matrix relationship. Consequently, when the matrix is imaged with $g = 10\bar{1}0$ reflection, the $g = 0002$ reflection of twins also activates. Fig. 7(a) and 7(b) shows WBDF TEM images of different regions of the same twin-twin intersection for the $g = 0002$ and $g = 10\bar{1}\bar{1}$ operating reflections of T1.

For the $g = 0002$ reflection of recipient twin T1, defects are visible, indicating that the defects inside the T1 have a strong $\langle c \rangle$ component. Moreover, the defect contrast lies parallel to the trace of the basal plane and is like the basal dislocation contrast seen in the matrix. To determine the nature of these $\langle c \rangle$-component defects, TEM dislocation contrast experiments is performed using various operating reflections. Fig. 8(a) shows the WBDF TEM images of a portion of twin T1 under different operating reflections. The invisibility cri-

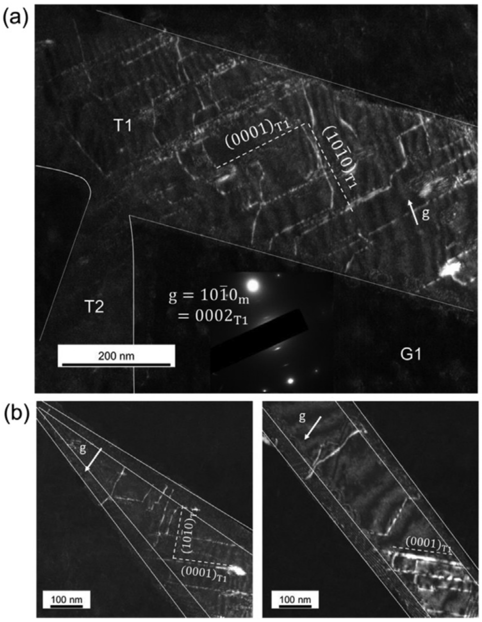

Fig. 7. WBDF TEM images showing the structure of dislocations inside twin T1. (a) The dislocations are visible for $g = 0002$ reflection, suggesting that they have a strong $\langle c \rangle$ component, and the dislocations are projected in different directions on the plane of the micrograph. (b) Shows there are a few non-basal $\langle c \rangle$ components inside T1 for $g = 10\bar{1}\bar{1}$. The solid lines in the micrographs represent the twin boundary.

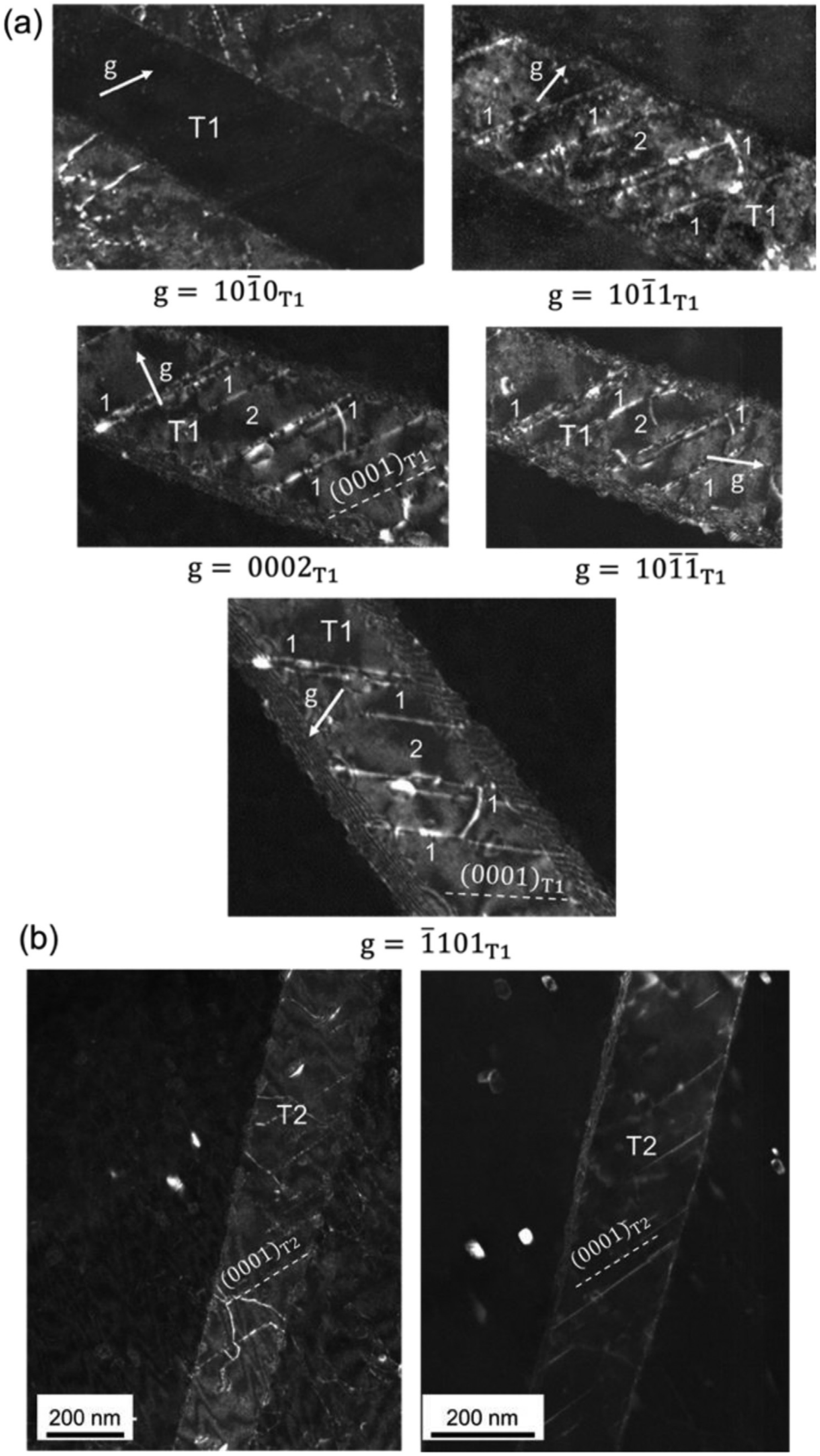

$g = 10\bar{1}0_{T1}$

$g = 10\bar{1}1_{T1}$

$g = 0002_{T1}$

$g = 10\bar{1}\bar{1}_{T1}$

$g = \bar{1}101_{T1}$

Fig. 8. (a) WBDF micrographs showing the variation in dislocation contrast in the domain of twin T1 for the various operating reflections. (b) The TEM images showing stacking fault contrast parallel to the trace of the basal plane after tilting the sample about the $[\bar{1}010]$ axis of twin T2.

teria analysis confirms that the defects labeled as “1” are ⟨c + a⟩ dislocations with Burgers vector $\frac{1}{3}[\bar{1}2\bar{1}3]$, which is also the Burgers vector of the ⟨c + a⟩ dislocations in the matrix. The defect labeled as “2” is visible only under $g = 10\bar{1}\bar{1}$ reflection and is invisible for all other reflections, suggesting that it is a pure edge dislocation with Burgers vector $\frac{1}{3}[\bar{2}110]$. A similar diffraction contrast analysis confirms that the same set of ⟨c + a⟩ dislocations, i.e., $\frac{1}{3}[\bar{1}2\bar{1}3]$, are present inside twin T2 as well.

Similar to the matrix dislocations, the observed ⟨c + a⟩ dislocations in Figs. 7 and 8 may be blocked at the line of intersection of the type-II pyramidal plane $(1\bar{2}12)$ and the basal plane (see Fig. 5(b)), along the $[\bar{1}010]$ direction, as evident by the line contrast parallel to the basal plane trace. These ⟨c + a⟩ dislocation segments, oriented horizontally in the image, are in edge orientation, with their observed Burgers vector $\frac{1}{3}[\bar{1}2\bar{1}3]$, perpendicular to the $[\bar{1}010]$ line direction. In contrast, the vertical dislocation segments are in near screw orientation. Fig. 8(b) shows the structure of the ⟨c + a⟩ dislocations inside twin T2. Like the matrix dislocations, these ⟨c + a⟩ edge dislocations exhibit a stacking fault contrast (Fig. 8(b)). As discussed in the previous sections, this stacking fault contrast is visible only when the sample is tilted slightly about the $[\bar{1}010]$ axis. However, in this case, the screw ⟨c + a⟩ dislocations did not dissociate into partial dislocations. No stacking fault contrast is in the right image in Fig. 8(b).

4. Discussion

Detailed TEM based analysis of deformed Mg-3wt.%Y alloy microstructures finds that the morphology of interacting twins is not symmetric. Type-II pyramidal ⟨c + a⟩ dislocations are present in the matrix grain and also inside the twin domains. In contrast, no ⟨a⟩ dislocations were observed in the matrix grain. A similar observation has been reported in a Mg-0.6wt.%Y alloy, however, for a twin free grain, where type-I pyramidal ⟨c + a⟩ matrix dislocations were observed without basal ⟨a⟩ slip [11]. In the current study the ⟨c + a⟩ matrix dislocations were found to lie on a type-II pyramidal plane and satisfy the slip system: $\frac{1}{3}[\bar{1}2\bar{1}3](1\bar{2}12)$. This abundant activity of ⟨c + a⟩ slip may be attributed to the Y alloying element, which is known to enhance ⟨c + a⟩ slip activity in Mg [26,45,46,56,57]. Nevertheless, the actual role of Y on the choice of type-I and type-II pyramidal slip systems is not well understood. For instance, Sandlobes et al. observed the presence of both type-I and type-II pyramidal ⟨c + a⟩ slip systems in a deformed Mg-3wt.%Y alloy [45]. Besides, the absence of basal ⟨a⟩ slip in G1 may be a consequence of the orientation of G1 with respect to the deformation loading. Moreover, the ⟨c + a⟩ dislocations in the current study exhibit a line contrast parallel to the trance of basal plane. This observation is consistent with the ⟨c + a⟩ dislocation contrast seen in earlier studies for pure Mg, Mg-3wt.%Y and Mg-Li alloys [26,45,54,55]. Further, the ⟨c + a⟩ dislocations concentrate at the TTJ site and interacts with the twin boundaries. The edge component of the ⟨c + a⟩ dislocations interact predominantly with the T2 twin boundary, whereas the screw components interact predominantly with the T1 twin boundary. In this section, these findings are rationalized using the crystal plasticity calculations and detailed crystallographic analysis.

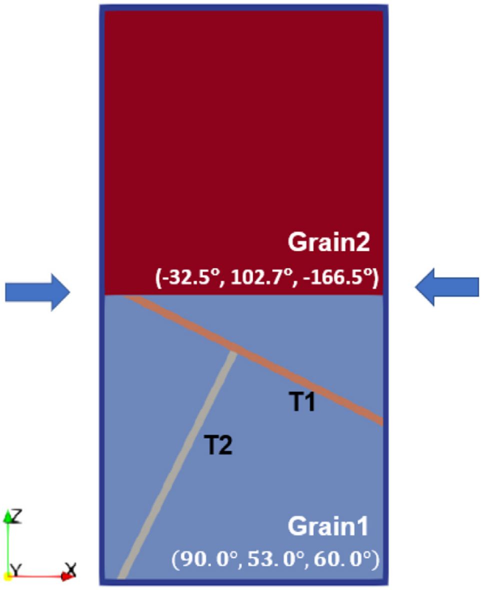

Fig. 9. Model arrangement for explicit simulation of twin-twin junction within an EVPFFT framework.

4.1. Crystal plasticity calculations

To understand the experimentally observed ⟨c + a⟩ dislocations inside and in the vicinity of the TTJs, spatially resolved stress field calculations are performed using the EVPFFT model. The microstructure model for calculation is developed to mirror the experimental microstructure shown in Fig. 3. The unit simulation cell is shown in Fig. 9 and is comprised of two grains surrounded by a buffer layer. The crystallographic orientations of G1 and G2, in Bunge convention, are (90.0°, 53.0°, 60.0°) and (−32.5°, 102.7°, −166.5°). As characterized experimentally, T1 is $(10\bar{1}2)[\bar{1}011]$ and T2 is $(\bar{1}012)[10\bar{1}1]$ lying inside the G1. Based on the crystallographic orientation of G1, the twinning plane normal and shear direction of both the twins lie within the XZ plane. To model the effect of the free surface, the out-of-plane shear in the XY and YZ planes is zero. This method for free-surface effects has been demonstrated to yield better agreement with TEM and EBSD surface measurements [58]. The unit cell is discretized into 1000 × 3 × 1000 voxels with periodic boundary conditions in all three directions. This fine voxel resolution provides the resolution needed for comparison with TEM and minimizes Gibbs oscillations. The thickness of both twin domains spans 11 voxels. The buffer layer with properties of a random texture material is 10 voxels thick and surrounds the grain in the XZ plane. Various buffer layer thicknesses have been tested and this one is shown to minimize image fields for the material response and applied deformation conditions.

Table 3
Crystallography of all six pyramidal slip systems that are considered in this work.

	Py1	Py2	Py3	Py4	Py5	Py6
Slip plane	(2-1-12)	(11-22)	(−12-12)	(−2112)	(−1-122)	(1-212)
Slip direction	[2-1-1-3]	[11-2-3]	[−12-1-3]	[−211-3]	[−1-12-3]	[1-21-3]

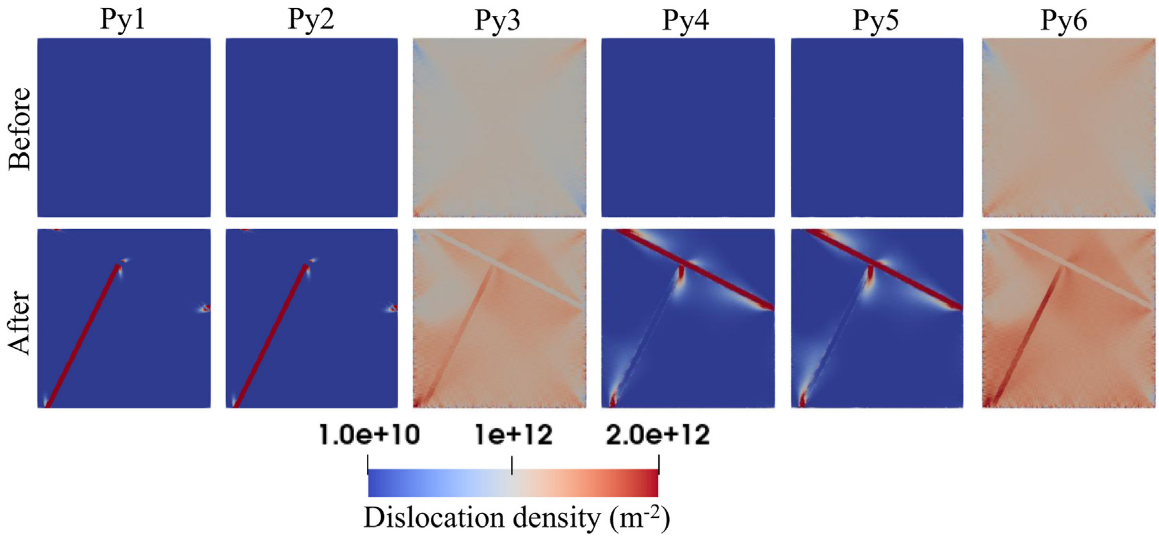

Fig. 10. Effect of twin-twin junction formation on pyramidal slip dislocation density distribution. The first and second rows present the dislocation fields before and after twinning, respectively, at 2% strain.

The simulation of twin-twin interaction is performed using the following sequence. First, the entire unit cell is compressed along the X-direction under a constant strain state (0.0001 1/s) and the boundaries in the Z and Y-directions are stress-free. At an applied strain of 2% the voxels lying within T1 and T2 are first reoriented to their corresponding twin variant. Then the characteristic twin shear of 13% for Mg is applied incrementally and homogeneously across each twin domain in 1000 steps.

4.2. Origin of pyramidal ⟨c+a⟩ dislocations in the matrix grain

To understand the experimentally observed dislocation distributions, the model calculated DD fields of all six pyramidal-II slip systems are analyzed here. Table 3 lists the crystallographic details these six pyramidal-II slip systems. Fig. 10 shows these fields within the parent G1, which includes the interacting twin domains. For comparison, the DD fields in the twin free crystal but generated under the same macroscopic strain are given in the first row and those with the TTJ in the second one. Following the convention in Table 3, the experimentally observed ⟨c + a⟩ system is Py6. The model indicates that macroscopic straining increases the DD of systems Py3 and Py6 to $\sim 1 \times 10^{12}$ and $\sim 1.5 \times 10^{12}$, respectively, from the initial DD of 1×10^{10} in the twin-free crystal. The experimentally observed Py6 slip dislocations in the grain G1, therefore, could have been generated independent of the TTJ. As described earlier, the model in this calculation included the neighboring grain G2. To test the effect of G2, another simulation without it is performed. Interestingly, systems Py1, 2, 4, and 5 are the most active compared to Py3 and Py6. The implication is that neighboring grain G2 and its interaction with G1 alter the stress field inside G1 in a way that favored activation of Py3 and Py6. Although not shown, the calculations confirm that the activation of basal ⟨a⟩ slip is not significant during the initial loading and also in the process of twin-twin junction formation.

4.3. Origin of pyramidal ⟨c+a⟩ dislocations inside the twin domains

Here, the source for the experimentally observed pyramidal dislocations inside the twin domains are analyzed. The second row in Fig. 10 shows the DD fields after forming the TTJ. It reveals that the DD of systems Py3 and Py6 increase around twins T1 and T2 in the matrix, and inside twin T2. Further, DD for systems Py1 and Py2 increased inside T2, whereas DD for systems Py4 and Py5 increased inside T1. The direct comparison of the first and second rows reveals that twinning promoted DD of systems Py1, 2, 4 and 5 more so than in systems Py3 and 6. However, the TEM analysis did not find these slip dislocations inside the twin domains. At the same time, although the predicted increase in Py6 agrees with the TEM observation, the percent increase for Py6 in the twin domains is relatively small. These model predictions suggest that the experimentally observed Py6 dislocations inside the twin domain did not develop due to the TTJ. Rather they are likely to be developed during the initial loading before twin-

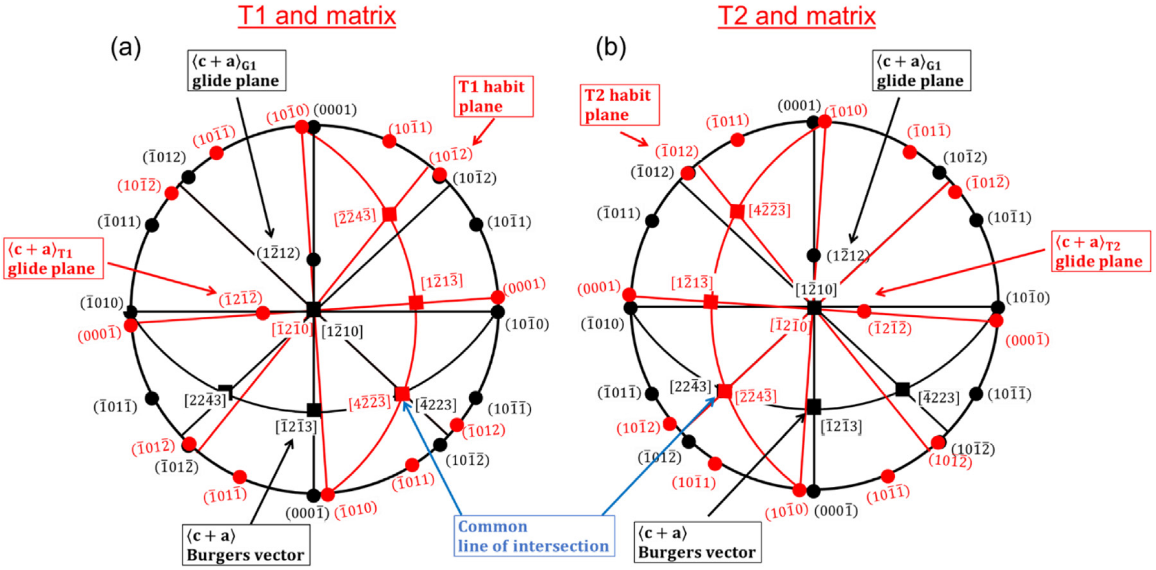

Fig. 11. Standard HCP stereographic projections showing the geometric relation between the $<c + a>$ slip glide planes and the habit planes of T1 and T2. The blue arrows indicate the common line of intersections that contain $<c + a>$ slip planes and the habit planes of T1 and T2. Consequently, the matrix $<c + a>$ dislocations may penetrate the twin boundaries of T1 and T2 along the common line of intersection and enter the twin domains under suitable stress concentrations.

ning and/or by dislocation transmission from the surrounding matrix into the twin domains.

The transmission of dislocations from the matrix to twin domains is possible only when there is a common line of intersection that contains the glide planes of dislocations (in the matrix and twin domains) as well as the twinning plane. Earlier studies suggest that the basal matrix ⟨a⟩ dislocations cross-slip directly into the tensile twin domain only if they are in screw orientation i.e., the Burgers vector of ⟨a⟩ dislocations is parallel to the line of intersection [12–15]. In contrast, the non-screw ⟨a⟩ dislocations may be absorbed by the twin boundary or may dissociate at the twin boundary and thereby generate twinning dislocations. The present investigations reveal that the ⟨c + a⟩ dislocations in the matrix as well as in the twin domains of TTJ belong to the same system, which is $\frac{1}{3}[\bar{1}2\bar{1}3](1\bar{2}12)$. The $(1\bar{2}12)$ glide planes intersect the T2 twinning plane, $(\bar{1}012)$ along the $[22\bar{4}3]$ direction, and the T1 twinning plane $(10\bar{1}2)$ along the $[\bar{4}223]$ direction. Thus, based on geometry, these ⟨c + a⟩ dislocations may penetrate the T1 and T2 twins along their corresponding common line of intersections and enter the twin domains under the appropriate stress conditions. While the requisite stresses cannot be quantified, the possibility of twin boundary transmission cannot be ignored. Fig. 11 shows these directions in terms of the standard HCP Mg stereographic projections for T1 and T2 twins, where the black and red traces represent the orientations of matrix and twins (T1, T2) respectively. The projections clearly show that $[\bar{4}223]$ and $[22\bar{4}3]$ (indicated by blue arrows) are common lines of intersections, which contain the traces corresponding to the glide planes of ⟨c + a⟩ dislocations as well as the habit planes of T1 and T2. However, the observed Burgers vector $\frac{1}{3}[\bar{1}2\bar{1}3]$ of ⟨c + a⟩ dislocations is found to be non-parallel to the line of intersections $[22\bar{4}3]$ and $[\bar{4}223]$, suggesting that the likelihood of cross-slip of matrix ⟨c + a⟩ dislocations into the twin domains along those common line of intersections is not high, and the dislocations could simply terminate at the boundaries of T1 and T2 as observed in Fig. 5(a). Based on these geometrical observations, it is possible to ascertain that the ⟨c + a⟩ dislocations inside the domains of TTJ did not originate from cross-slip of matrix dislocations and they may have formed because of macroscopic deformation conditions used in this study.

4.4. Nature of pyramidal ⟨c + a⟩ *dislocations in the vicinity of TTJ*

Results in the current study revealed that the matrix ⟨c + a⟩ dislocations interacting with the twin boundaries of TTJ in a particular orientation (see Fig. 5(a)). The ⟨c + a⟩ dislocations interacting with the recipient (T1) twin boundary were found to be predominantly in a near-screw orientation, whereas the ⟨c + a⟩ dislocations interacting with the impinging (T2) twin boundary were in an edge orientation. This may be visualized by imagining a ⟨c + a⟩ dislocation in the form of a loop on the type-II pyramidal plane $(1\bar{2}12)$ as shown schematically in Fig. 12(a). The red colored arrows indicate the projected direction of the Burgers vector of ⟨c + a⟩ dislocations, i.e., $\frac{1}{3}[\bar{1}2\bar{1}3]$ on the plane of the paper. Geometrically the normal of $(1\bar{2}12)$ makes an angle of 58.5° with the [0001] direction, and it also contains the $[\bar{1}010]$ direction of the matrix as shown in the inset. Under appropriate loading conditions, the ⟨c + a⟩ loop could have expanded and intersected with the boundaries of T1 and T2 as illustrated schematically in Fig. 12(b). This could result in a screw orientation of ⟨c + a⟩ dislocations for the recipient twin T1 because the Burgers vector is nearly parallel to the line segment of ⟨c + a⟩ dis-

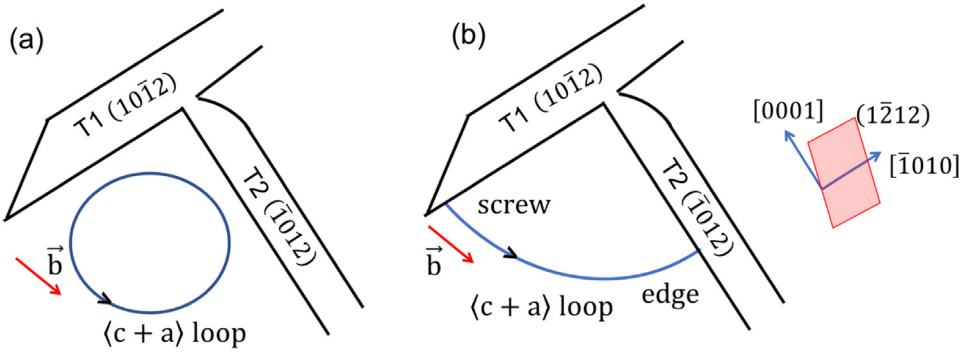

Fig. 12. A schematic illustrating a situation where a ⟨c + a⟩ dislocation loop (under suitable stress concentrations) expands and interact with the boundaries of T1 and T2 in screw and edge orientations. This could result in a situation described in Fig. 5(a). The red arrows in the schematic indicate the projected direction of the observed Burgers vector on the plane of the paper. The inset shows the relation between matrix directions and the glide plane of ⟨c + a⟩ dislocations, where the normal of the glide plane makes angle of 58.5° with the [0001] direction.

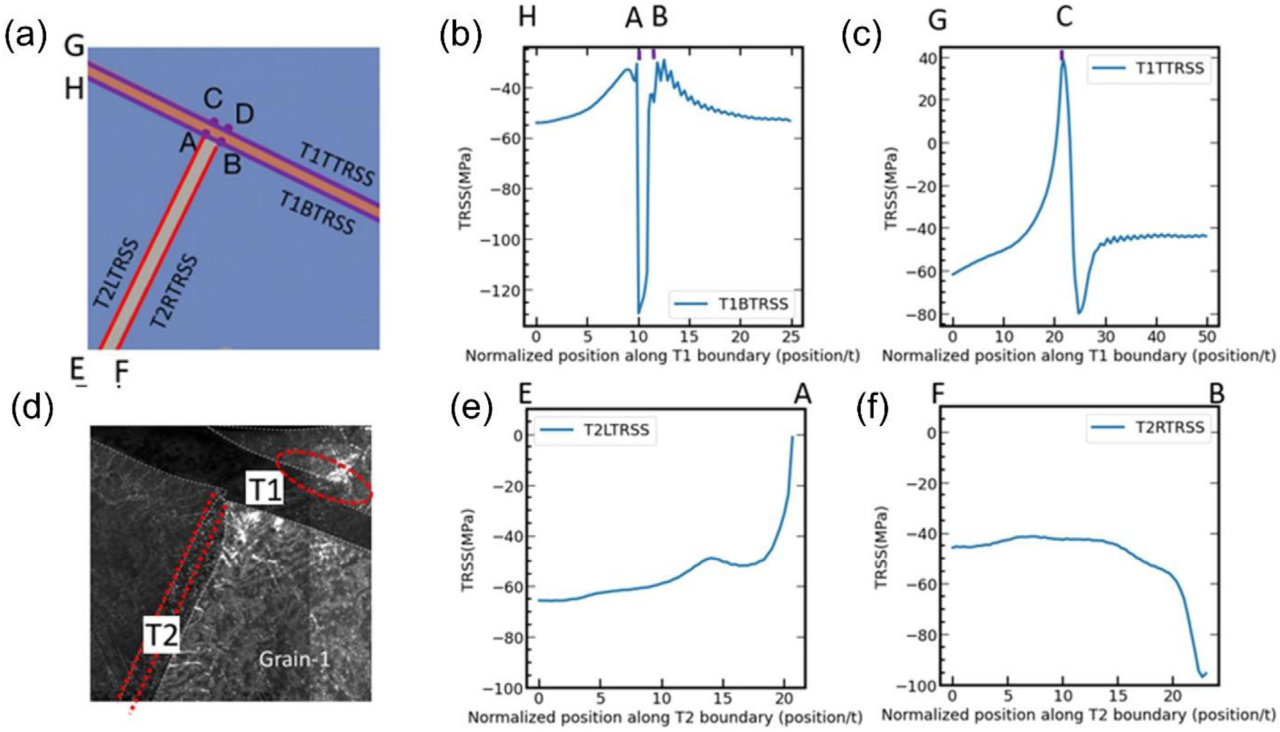

Fig. 13. Distribution of TRSS fields after twin-twin junction formation. (a) Simulated and (d) experimentally observed twin-twin junction. Key locations (A to H) are marked in (a). T1-TRSS profile along the (b) top and (c) bottom interface of T1. T2-TRSS profile along the (e) left and (f) right interface of T2.

locations (see Fig. 12(b)). In contrast, at the impinging twin T2 boundary, the ⟨c + a⟩ dislocations exhibit edge character because their line direction is perpendicular to the observed Burgers vector.

Further, the TEM images provided evidence of loop contrast for ⟨c + a⟩ dislocations on the basal plane of Mg-3wt.%Y alloy and is consistent with the loop contrast observed in earlier studies [59–61]. It was suggested that the ⟨c + a⟩ dislocations gliding on type-II pyramidal plane could be dissociated into partial dislocations bounding a stacking fault. It is, therefore, reasonable to assume that the ⟨c + a⟩ dislocations observed in the current study are dissociated into partial dislocations bounding a stacking fault on the basal plane. Although an explicit investigation has not be performed in this study to identify the stacking fault vectors, the earlier reports suggest the following dissociation mechanism that could lead to the appearance of stacking fault contrast on the basal plane [59].

$$\frac{1}{3}[2\bar{1}\bar{1}3] \rightarrow \frac{1}{6}[2\bar{2}03] + SF_{(0001)} + \frac{1}{6}[20\bar{2}3]$$

Based on this reaction, here one can speculate a similar type of dissociation reaction may have produced the basal stacking fault contrast seen in Figs. 6 and 8(b). In contrast to the edge ⟨c + a⟩ dislocations, the near-screw ⟨c + a⟩ dislocation segments do not show such a stacking fault contrast, as confirmed by the absence of non-basal stacking fault contrast in Fig. 6(b). The same conclusions can be made in Fig. 6(c) and (d), where the ⟨c + a⟩ dislocations interacting with the T2 twin tip also exhibit basal stacking fault contrast. From Fig. 6(b) the stacking fault density is higher at the T2 twin boundary. This is because the ⟨c + a⟩ dislocations interacting with the T2 twin are predominantly in edge orientation (see Fig. 6(a)). In contrast, the ⟨c + a⟩ dislocations interacting with the T1 are predominantly in screw orientation, and like before, these screw ⟨c + a⟩ dislocations are not widely dissociated enough to show any stacking fault contrast. Consequently, the stacking fault density is lower on the T1 side.

4.5. Local stresses and growth of interacting twins

In this section, the local stress field in the vicinity of the TTJ is studied to understand the experimentally observed morphology of the interacting twins. The EVPFFT model provides the full stress and strain tensor fields at every strain level. Using the full stress tensor, the resolved shear stress along the twinning shear direction (TRSS) is calculated to understand whether the local stress fields favor the twin boundary migration. The TRSS on the interface can drive the twin dislocation to glide along a coherent twin boundary or the basal-prism facets, resulting in twin boundary migration [62–64]. In the following description, T1-TRSS and T2-TRSS represent the resolved shear stress along the T1 shear direction and T2 shear direction, respectively. The TRSS fields in the matrix near the twin interface (the purple and red lines shown in Fig. 13(a)) are plotted in Fig. 13(b,c,e,f). Fig. 13(b) shows a negative (anti-twinning) T1-TRSS along the entire profile of the T1 bottom interface. Thus, the T1 boundary migration is not favored on the lower side. On the other hand, Fig. 13(c) shows that there is a small region on the left of point C where T1-TRSS is positive, while there is a sudden decrease in the T1-TRSS on the right side of point C. This indicates that with further compression, the T1 top interface may undergo asymmetric growth, initiating growth on the left. One could use this asymmetric stress profile to understand the experimentally observed step-like feature in the TEM image (see the red circle in Fig. 13(d)).

In Fig. 13(e) and (f), the T2-TRSS is negative on both sides of T2, which suggests that the twin boundary migration on both sides of T2 is not favored. However, with further macroscopic loading, the twin boundary migration could result in an asymmetric growth of T2 since the resisting anti-twinning T2-TRSS on the left side is much larger than that on the right side. Meanwhile, a steep decline of T2-TRSS in Fig. 13(f) near point B implies that the twin boundary close to this site will be subjected to a larger resistance than other regions. This explains the sharp geometry of the T2 tip marked in Fig. 11(d). In summary, the twin-twin interaction-induced stress fields suggest that the migration of the T1 top boundary can create a non-smooth stepped boundary as observed experimentally in Fig. 4.

5. Summary and conclusions

In this work, a combined experimental and numerical analysis is performed to understand the local defects within and in the vicinity of twin-twin junctions (TTJs). Cozone $\{10\bar{1}2\}$ tensile twins in a deformed Mg-3wt.%Y alloy are selected for analysis. TEM analyses are employed to characterize the local defect structures in the vicinity of the TTJs as well as in the twin domains. To understand and rationalize the experimental observations, the crystal plasticity EVPFFT framework is used. The model microstructure of the TTJs is generated to match the experimentally observed TTJ microstructure, including the parent and neighboring grain orientations. The key findings from this combined experimental/modeling study are as follows:

- A high density of ⟨c + a⟩ dislocations is observed in the matrix surrounding the TTJ where the two twins meet. The same ⟨c + a⟩ dislocations have also been found inside the interacting twin domains, and some of these dislocations appear to have crossed the twin boundary. No pure ⟨a⟩ dislocations are observed in the matrix regions. A similar observation, i.e., the activation of ⟨c + a⟩ dislocations without any ⟨a⟩ dislocations, has been observed in Mg-0.6wt.%Y alloy also [11].
- The observed ⟨c + a⟩ dislocations in matrix grain exhibit a line contrast parallel to the trance of basal plane. A similar observation has been reported in pure Mg, Mg-3wt.%Y, and Mg-Li alloys [26,45,54,55].
- The observed ⟨c + a⟩ dislocations in both the matrix and interacting twins are $\frac{1}{3}[\bar{1}2\bar{1}3](1\bar{2}12)$, classified as type-II pyramidal dislocations. These dislocations have been observed in both the edge and screw orientations. The matrix ⟨c + a⟩ dislocations interacting with the impinging twin boundary are predominantly edge. In contrast, those that interact with the recipient twin boundary are predominantly screw. The edge dislocations are dissociated into partials while the screw dislocations are not.
- A detailed geometrical analysis of the dislocations and twins' crystallography suggests that the observed ⟨c + a⟩ dislocations inside the domains of TTJ did not transmit from the matrix grain, instead, they may have formed by the imposed macroscopic loading.
- The model calculations show that the twin-twin interactions increase the density of experimentally observed pyramidal ⟨c + a⟩ dislocations in the matrix domain, but not in the interacting twin domains. This implies that the experimentally seen pyramidal ⟨c + a⟩ dislocations in the twin domains most likely formed in the matrix during macroscopic loading before the TTJ formed and after the formation of twin domains, but not as a result of the TTJ.
- The model calculated local stresses suggest that the impinging twin will undergo an asymmetric growth process, which rationalizes the experimentally observed asymmetric twin morphology. Further, the local stress concentration in the recipient twin boundary explains the experimentally observed stepped features in its top boundary.

Overall, this work clearly shows that the twin-twin interactions can develop a high density of dislocations and stress concentrations in the localized regime near a TTJ. These local fields are signatures of how the twin and microstructure would evolve in the presence of TTJs and in turn how TTJs affect macroscopic response. Such consequences of twin-twin interactions are non-negligible and hence need to be considered when attempting to understand and predict the deformation response of HCP Mg and its alloys. Specifically, these local defect details need to be accounted for in mechanistic constitutive laws that aim to capture the effect of twin-twin and twin-dislocation interactions [65–70]. It will certainly improve the predictability of the models on the aspect of mechanical responses like strain hardening and also damage/failure behavior.

Declaration of Competing Interest

The authors declare that they have no known competing financial interests or personal relationships that could have appeared to influence the work reported in this paper.

Acknowledgment

M.A.K. acknowledges support from the U.S. Dept. of Energy, Office of Basic Energy Sciences Project FWP 06SCPE401. J.W. and I.J.B. acknowledge support from the National Science Foundation under Grant Number 2051390. K.Y. acknowledges the financial support from the National Science Foundation CMMI-1723539. X.W., T.J.R, E.J.L., and J.M.S. acknowledge the financial support from the National Science Foundation CMMI-1729829.

References

[1] M.K. Kulekci, Int. J. Adv. Manuf. Technol. 39 (9–10) (2008) 851–865.
[2] P.G. Partridge, Metall. Rev. 12 (1967) 169–194.
[3] M.H. Yoo, Metall. Trans. A Phys. Metall. Mater. Sci. 12 (3) (1981) 409–418.
[4] M.R. Barnett, Mater. Sci. Eng. A Struct. Mater. Prop. Microstruct. Process. 464 (1–2) (2007) 1–7.
[5] I.J. Beyerlein, L. Capolungo, P.E. Marshall, R.J. McCabe, C.N. Tome, Philos. Mag. 90 (30) (2010) 4073–4074.
[6] J.P. Hirth, J. Lothe, Theory of Dislocations, 2nd ed., Krieger Pub. Co., Malabar, FL, 1992.
[7] M. Zaiser, M.C. Miguel, I. Groma, Phys. Rev. B 64 (22) (2001) 224102.
[8] R. Madec, B. Devincre, L. Kubin, T. Hoc, D. Rodney, Science 301 (5641) (2003) 1879–1882.
[9] G. Monnet, B. Devincre, L. Kubin, Acta Mater. 52 (14) (2004) 4317–4328.
[10] R. Madec, B. Devincre, L.P. Kubin, Phys. Rev. Lett. 89 (25) (2002).
[11] K. Yaddanapudi, B. Leu, M.A. Kumar, X. Wang, J.M. Schoenung, E.J. Lavernia, T.J. Rupert, I.J. Beyerlein, S. Mahajan, Acta Mater. 204 (2021) 116514.
[12] P. Chen, F. Wang, B. Li, Acta Mater. 164 (2019) 440–453.
[13] J. Zhang, G. Xi, X. Wan, C. Fang, Acta Mater. 133 (2017) 208–216.
[14] F. Wang, C.D. Barrett, R.J. McCabe, H. El Kadiri, L. Capolungo, S.R. Agnew, Acta Mater. 165 (2019) 471–485.
[15] M. Gong, G. Liu, J. Wang, L. Capolungo, C.N. Tomé, Acta Mater. 155 (2018) 187–198.
[16] M. Gong, W. Wu, J. Mater. Res. 35 (13) (2020) 1647–1659.
[17] N. Bertin, C.N. Tome, I.J. Beyerlein, M.R. Barnett, L. Capolungo, Int. J. Plast. 62 (2014) 72–92.
[18] M. Ardeljan, I.J. Beyerlein, M. Knezevic, Int. J. Plast. 99 (2017) 81–101.
[19] L. Capolungo, I.J. Beyerlein, G.C. Kaschner, C.N. Tome, Mater. Sci. Eng. A Struct. Mater. Prop. Microstruct. Process. 513-14 (2009) 42–51.
[20] A. Serra, D.J. Bacon, Philos. Mag. A Phys. Condens.Matter Struct. Defects Mech. Prop. 73 (2) (1996) 333–343.
[21] D. Spearot, L. Capolungo, C. Tomé, Phys. Rev. Mater. (2019) (Accepted for publications).
[22] F. Wang, S.R. Agnew, Int. J. Plast. 81 (2016) 63–86.
[23] A. Serra, D. Bacon, Acta Metall. Mater. 43 (12) (1995) 4465–4481.
[24] N. Zhou, Z. Zhang, L. Jin, J. Dong, B. Chen, W. Ding, Mater. Des. 56 (2014) 966–974 1980-2015.
[25] H. Su, X. Zhou, M. Zhang, S. Zheng, H. Ye, Z. Yang, Acta Mater. 206 (2021) 116622.
[26] S. Agnew, J. Horton, M. Yoo, Metall. Mater. Trans. A 33 (3) (2002) 851–858.
[27] J. Xu, B. Guan, H. Yu, X. Cao, Y. Xin, Q. Liu, J. Mater. Sci. Technol. 32 (12) (2016) 1239–1244.
[28] G.L. Shi, K. Zhang, X.G. Li, Y.J. Li, M.L. Ma, J.W. Yuan, H.J. Zhang, J. Magnes. Alloy. (2021).
[29] D. Shi, C. Wang, C. Cepeda-Jimenez, M.T. Pérez-Prado, Acta Mater. 221 (2021) 117442.
[30] E. Roberts, P. Partridge, Acta Metall. 14 (4) (1966) 513–527.
[31] L. Jiang, J.J. Jonas, A.A. Luo, A.K. Sachdev, S. Godet, Mater. Sci. Eng. A 445 (2007) 302–309.
[32] Q. Yu, Y. Jiang, J. Wang, Scr. Mater. 96 (2015) 41–44.
[33] Q. Yu, J. Wang, Y.Y. Jiang, R.J. McCabe, N. Li, C.N. Tome, Acta Mater. 77 (2014) 28–42.
[34] H. El Kadiri, J. Kapil, A.L. Oppedal, L.G. Hector, S.R. Agnew, M. Cherkaoui, S.C. Vogel, Acta Mater. 61 (10) (2013) 3549–3563.
[35] F. Mokdad, D.L. Chen, D.Y. Li, J. Alloy. Compd. 737 (2018) 549–560.
[36] B.M. Morrow, E.K. Cerreta, R.J. McCabe, C.N. Tome, Mater. Sci. Eng. A Struct. Mater. Prop. Microstruct. Process. 613 (2014) 365–371.
[37] B.M. Morrow, R.J. Mccabe, E.K. Cerreta, C.N. Tome, Metall. Mater. Trans. A Phys. Metall. Mater. Sci. 45a (1) (2014) 36–40.
[38] W.D. Russell, N.R. Bratton, Y. Paudel, R.D. Moser, Z.B. McClelland, C.D. Barrett, A.L. Oppedal, W.R. Whittington, H. Rhee, S. Mujahid, Metals 10 (11) (2020) 1403 (Basel).
[39] Q. Yu, J. Zhang, Y. Jiang, Mater. Sci. Eng. A 528 (25–26) (2011) 7816–7826.
[40] M. Gong, S. Xu, Y. Jiang, Y. Liu, J. Wang, Acta Mater. 159 (2018) 65–76.
[41] M.A. Kumar, M. Gong, I. Beyerlein, J. Wang, C.N. Tomé, Acta Mater. 168 (2019) 353–361.
[42] J. Lloyd, J. Ligda, C. Williams, Materialia 9 (2020) 100606.
[43] K. Zhang, Z. Shao, J. Jiang, Mater. Des. 194 (2020) 108936.
[44] Q. Sun, X. Zhang, Y. Ren, L. Tan, J. Tu, Mater. Charact. 109 (2015) 160–163.
[45] S. Sandlöbes, M. Friák, J. Neugebauer, D. Raabe, Mater. Sci. Eng. A 576 (2013) 61–68.
[46] S. Sandlöbes, M. Friák, S. Zaefferer, A. Dick, S. Yi, D. Letzig, Z. Pei, L.-F. Zhu, J. Neugebauer, D. Raabe, Acta Mater. 60 (6–7) (2012) 3011–3021.
[47] N. Stanford, R.K.W. Marceau, M.R. Barnett, Acta Mater. 82 (2015) 447–456.
[48] J. Wang, X. Wang, K. Yu, T.J. Rupert, S. Mahajan, E.J. Lavernia, J.M. Schoenung, I.J. Beyerlein, Mater. Sci. Eng. A 817 (2021) 141373.
[49] R.A. Lebensohn, A.K. Kanjarla, P. Eisenlohr, Int. J. Plast. 32-33 (2012) 59–69.
[50] M.A. Kumar, A.K. Kanjarla, S.R. Niezgoda, R.A. Lebensohn, C.N. Tome, Acta Mater. 84 (2015) 349–358.
[51] M.A. Kumar, I.J. Beyerlein, C.N. Tome, Acta Mater. 116 (2016) 143–154.
[52] I.J. Beyerlein, C.N. Tome, Int. J. Plast. 24 (5) (2008) 867–895.

[53] G. Simmons, H. Wang, Single Crystal Elastic Constants and Calculated Aggregate properties: A Handbook, MIT press, 1971.

[54] T. Obara, H. Yoshinga, S. Morozumi, Acta Metall. 21 (7) (1973) 845–853.

[55] J. Geng, M. Chisholm, R. Mishra, K. Kumar, Philos. Mag. 95 (35) (2015) 3910–3932.

[56] M. Lentz, M. Klaus, R.S. Coelho, N. Schaefer, F. Schmack, W. Reimers, B. Clausen, Metall. Mater. Trans. A Phys. Metall. Mater. Sci. 45a (12) (2014) 5721–5735.

[57] Z. Ding, W. Liu, H. Sun, S. Li, D. Zhang, Y. Zhao, E.J. Lavernia, Y. Zhu, Acta Mater. 146 (2018) 265–272.

[58] B. Leu, M.A. Kumar, I.J. Beyerlein, Materialia 17 (2021) 101124.

[59] J. Geng, M.F. Chisholm, R. Mishra, K. Kumar, Philos. Mag. Lett. 94 (6) (2014) 377–386.

[60] B. Li, P. Yan, M. Sui, E. Ma, Acta Mater. 58 (1) (2010) 173–179.

[61] B. Li, Q. Zhang, S. Mathaudhu, Scr. Mater. 134 (2017) 37–41.

[62] J.W. Christian, S. Mahajan, Prog. Mater Sci. 39 (1–2) (1995) 1–157.

[63] A. Ostapovets, A. Serra, Philos. Mag. 94 (25) (2014) 2827–2839.

[64] J. Wang, L. Liu, C.N. Tome, S.X. Mao, S.K. Gong, Mater. Res. Lett. 1 (2) (2013) 81–88.

[65] A. Fernández, A. Jérusalem, I. Gutiérrez-Urrutia, M. Pérez-Prado, Acta Mater. 61 (20) (2013) 7679–7692.

[66] S.R. Kalidindi, A.A. Salem, R.D. Doherty, Adv. Eng. Mater. 5 (4) (2003) 229 -+.

[67] A.A. Salem, S.R. Kalidindi, R.D. Doherty, S.L. Semiatin, Mater. Sci. 37a (1) (2006) 259–268.

[68] G. Proust, C.N. Tome, A. Jain, S.R. Agnew, Int. J. Plast. 25 (5) (2009) 861–880.

[69] H. El Kadiri, A. Oppedal, J. Mech. Phys. Solids 58 (4) (2010) 613–624.

[70] A.L. Oppedal, H. El Kadiri, C.N. Tome, G.C. Kaschner, S.C. Vogel, J.C. Baird, M.F. Horstemeyer, Int. J. Plast. 30-31 (2012) 41–61.